

wind stress curl changes is a delayed process and would retard the existing cyclonic circulation. We would expect this influence to manifest itself with large reversals in PC1 of the geostrophic velocity like the variations in the curl PC1 or NAO with a 3- to 5-year delay. Figure 5C shows that there are peaks in geostrophic velocity PC1 with such a delay, but they are small relative to the overwhelming background trend.

Property 3 of the continuous weakening of the subpolar air-sea heat loss is consistent with the observations that deep convective conditions in the Labrador Sea have been absent since the early 1990s. Although changes in advection of heat can have as much as 50% effect on the subpolar heat storage changes (10), the local heat flux changes are still important, particularly in forcing deep convection. Because deep convection maintains a cold core around which lighter water masses circulate, cessation of deep convection would lead to a decaying baroclinic gyre. This decaying cold core of the Labrador Gyre from 1992 to 2002 is observable in the dynamic height increase (using WOCE section AR7/W), which is about 6 cm relative to 1000db (Fig. 1A) (fig. S3) and comparable with the altimeter SSH change. The strong height gradient associated with boundary currents is important to inferences of circulation; this is seen in the hydrography (fig. S3). Evidence from the hydrographic data together with the 1990s heat flux trend is supportive of a connection between convective forcing and the observed decline in the gyre strength. It might not have been the case if wind-driven barotropic circulation or overflow-driven circulation variability were dominant causes.

Conclusions. Altimetric geostrophic circulation observations and supporting deep-sea current-meter observations suggest significant changes over the last two decades, with increasing SSH and weakening subpolar gyre circulation in the 1990s. By comparing the dynamic consequences of three mechanisms, buoyancy forcing and barotropic and baroclinic response to local wind stress curl, we find that the gyre weakening in the 1990s is not attributable to local wind stress changes associated with NAO. The weakening-gyre scenario of the 1990s parallels the warming in the central subpolar gyre, which is the well-observed relaxation of the water column following the intense winter convection period of 1989–1994. The lack of deep convection is the oceanic response to the local buoyancy forcing, which has mimicked low-NAO heat fluxes even though the index itself has reversed itself twice during the 1990s.

Because we lack SSH data before 1978, we cannot determine whether the 1990s slowing gyre is a part of a decadal cycle or the beginning of a longer term trend. Because Labrador Sea processes are intimately linked to the meridional overturning circulation, involving both intermediate-depth and deep waters, these observations of rapid climatic

changes over one decade may merit some concern for the future state of the MOC. Continuation of the altimeter missions will allow us to follow the evolution of this subpolar signal and its influence on the North Atlantic. Field observations of the subsurface oceanic circulation, hydrography, and ice cover (28) will be of great importance in establishing the origin of these climate shifts.

References and Notes

1. J. W. Hurrell, *Science* **269**, 676 (1995).
2. R. R. Dickson *et al.*, *Nature* **416**, 832 (2002).
3. J. R. N. Lazier *et al.*, *Deep-Sea Res.* **49**, 1819 (2002).
4. C. Deser, M. L. Blackmon, *J. Clim.* **6**, 1743 (1993).
5. G. Reverdin, D. Cayan, Y. Kushnir, *J. Geophys. Res.* **102**, 8505 (1997).
6. I. M. Belkin, S. Levitus, J. Antonov, S.-A. Malmberg, *Prog. Oceanogr.* **41**, 1 (1998).
7. R. G. Curry, M. S. McCartney, *J. Phys. Oceanogr.* **31**, 3374 (2001).
8. R. R. Dickson, J. Meincke, S.-A. Malmberg, A. J. Lee, *Prog. Oceanogr.* **20**, 103 (1988).
9. G. Han, C. L. Tang, *J. Phys. Oceanogr.* **31**, 199 (2001).
10. N. Verbrugge, G. Reverdin, *J. Phys. Oceanogr.* **33**, 964 (2003).
11. M. K. Flatau, L. Talley, P. P. Niiler, *J. Clim.* **16**, 2355 (2003).
12. B. Hansen, W. Turrell, S. Osterhus, *Nature* **411**, 927 (2001).
13. R. S. Pickart *et al.*, *Nature* **424**, 152 (2003).
14. A. S. Bower *et al.*, *Nature* **419**, 603 (2002).
15. M. A. White, K. J. Heywood, *J. Geophys. Res.* **100**, 24931 (1995).
16. J. Cuny, P. B. Rhines, P. P. Niiler, S. Bacon, *J. Phys. Oceanogr.* **32**, 627 (2002).
17. D. M. Fratantoni, *J. Geophys. Res.* **106**, C1022067 (2001).
18. The RAFOS floats (14) highlight meridional pathways at depths ranging from near-surface to 1500 m. White and Heywood (15) argued from early altimeter data that changing winds can shift the site of northward flow; Cuny *et al.* (16) and Fratantoni (17) compared surface drifter data with satellite altim-

- etry, yet data density was not sufficient to show significant changes between the 1990s and 1980s.
19. S. Häkkinen, *J. Geophys. Res.* **106**, 13837 (2001).
 20. C. Eden, J. Willebrand, *J. Clim.* **14**, 2266 (2001).
 21. R. Döscher, C. W. Böning, P. Herrmann, *J. Phys. Oceanogr.* **24**, 2306 (1994).
 22. W. M. Smethie, R. A. Fine, *Deep-Sea Res.* **48**, 189 (2001).
 23. Mapping the distribution of natural and human-made trace chemicals is an "accurate" way to view the MOC [see, e.g., (22)].
 24. The "normal" heat flux pattern corresponding to NAO has the Labrador Sea out of phase with the Greenland-Norwegian Sea (29), but the eastward migration of the Icelandic Low has altered this relationship since 1995.
 25. P. B. Rhines, *J. Fluid Mech.* **37**, 161 (1969).
 26. R. J. Greatbatch, A. D. Goulding, *J. Phys. Oceanogr.* **19**, 572 (1989).
 27. Wind-driven currents are set up by propagation of topographic Rossby waves along f/h (Coriolis frequency/total depth) contours, eventually approximating a topographic-Sverdrup balance. This produces over a matter of a few weeks a single anticyclonic gyre, or "intergyre," centered at 50°N latitude, at the boundary between subpolar and subtropical gyres. The Mid-Atlantic Ridge dominates this f/h waveguide (25, 26).
 28. The Arctic-SubArctic Flux Program (ASOF) (<http://asof.npolar.no>) is an observational campaign bridging programs such as SEARCH and CLIVAR.
 29. R. R. Dickson *et al.*, *Prog. Oceanogr.* **38**, 241 (1996).
 30. Supported by the NASA Physical Oceanography Program (S.H.) and by the NOAA Arctic Research Office, Vetlesen Foundation, and the NSF Office of Polar Programs (P.B.R.). The Office of Naval Research and Bedford Institute of Oceanography supported the current-meter measurements. We thank J. R. N. Lazier, I. Yashayev, and J. Cuny for help with the subsurface ocean data, and D. Worthen for assistance with graphics.

Supporting Online Material

www.sciencemag.org/cgi/content/full/304/5670/555/DC1
Figs. S1 to S3

19 December 2003; accepted 20 March 2004

Synfire Chains and Cortical Songs: Temporal Modules of Cortical Activity

Yuji Ikegaya,^{1*} Gloster Aaron,^{1*} Rosa Cossart,¹
Dmitriy Aronov,¹ Ilan Lampl,² David Ferster,² Rafael Yuste^{1†}

How can neural activity propagate through cortical networks built with weak, stochastic synapses? We find precise repetitions of spontaneous patterns of synaptic inputs in neocortical neurons in vivo and in vitro. These patterns repeat after minutes, maintaining millisecond accuracy. Calcium imaging of slices reveals reactivation of sequences of cells during the occurrence of repeated intracellular synaptic patterns. The spontaneous activity drifts with time, engaging different cells. Sequences of active neurons have distinct spatial structures and are repeated in the same order over tens of seconds, revealing modular temporal dynamics. Higher order sequences are replayed with compressed timing.

The essence of cortical function is the propagation and transformation of neuronal activity by the cortical circuit (1). How activity can propagate through a network composed of weak, stochastic, and depressing synapses is, however, poorly understood (2–4). It has been proposed that sequences of synchronous activity ("synfire chains") propagate through

the cortical circuit with high temporal fidelity (5, 6). Synchronous summation of excitatory postsynaptic potentials (EPSPs) could ensure postsynaptic firing and the nonlinear gain caused by the spike threshold could preserve temporal fidelity, so reactivations of the same chain would result in exact repetitions of precise firing patterns (7). Repetitions of

temporally precise firing sequences of spikes have been reported (7, 8), although their existence is controversial (9).

If synfire chains, or precisely timed repetitions of spike sequences, exist in cortical activity, the reactivation of the same spatio-temporal pattern of activity should produce, as its postsynaptic signature, repetitions of patterns of synaptic activity in intracellular recordings from single neurons in the network. If a recorded neuron receives connections from cells located at different points in a chain, it will receive temporally stereotypical patterns of excitatory and inhibitory postsynaptic potentials (EPSPs and IPSPs) as the chain repeats its pattern of spikes. We searched systematically for repeated patterns of spontaneous synaptic inputs in pyramidal

neurons, using intracellular recordings from slices of mouse primary visual cortex or from intact cat primary visual cortex *in vivo* (10).

Precisely repeating motifs of spontaneous synaptic activity in slices. To detect repetitions of spontaneous activity, we calculated the covariance between any two segments of an intracellular recording (11), with low- (1 s; low resolution index, LRI) and high- (20 ms; high resolution index, HRI) resolution windows of analysis (fig. S1). The low-resolution window was used to identify regions of the traces with potential repeats; these regions were then scanned at high resolution. In 20 voltage-clamp recordings of spontaneous activity from slices (8 min long), we encountered repetitions of sequences of spontaneous activity with high HRI values and marked similarity in the patterns of positive and negative deflections in the membrane current ("motifs") (Fig. 1). Because recordings were taken at -70 mV, most repeated patterns were composed of EPSCs (5 to 20 pA). A total of 17,055 motifs passing minimum thresholds for HRI were found in 18 out of 20 cells (Fig. 1A), and different statistical analyses confirmed that they were not due to chance (fig.

S2, A to C). Moreover, motifs above chance level were not found in recordings of miniature EPSCs in slices under $1 \mu\text{M}$ tetrodotoxin (fig. S2, D and E) [control artificial cerebrospinal fluid (ACSF) HRI = 1.24 ± 0.74 , $n = 16,271$ motifs, 18 cells versus tetrodotoxin HRI = 0.70 ± 0.39 , $n = 1300$, 7 cells; $P < 0.01$]. Most (95.4%) motifs occurred in the absence of oscillations, as defined by whether or not a motif passed the minimum threshold for HRI when it was shifted by a putative oscillation period. The number of motifs per cell ranged from 0 to 7803, with a median of 143 motifs and HRIs ranging from 0.11 to 7.10 (mean HRI = 1.24 ± 0.74 , $n = 16,271$ motifs). The average interval between motif repetitions was 156.2 ± 113.1 s, ranging from 0.7 to 478.1 s. The average duration of a motif was 1006 ± 424 ms. In 11 out of 18 cells, motifs repeated three or more times (Fig. 1B). Although a motif could last more than 1 s and be repeated after several minutes, individual EPSCs repeated with an accuracy of better than 1 ms (Fig. 1, A and B, insets). In the 10 cells with highest HRIs, there were 4.6 ± 1.5 motifs per cell that displayed at least three postsynaptic currents (PSCs) that repeated with better than 1-ms precision. Repeating within 2-ms precision, there were 53.7 ± 22.2 motifs per cell that had at least three such precise PSCs. Finally, in simultaneously recorded neurons, repeats of intracellular motifs sometimes occurred exactly at the same time (three out of six cell pairs; 15.4 ± 3.7 simultaneous motifs per cell pair).

Repeating motifs of spontaneous synaptic activity *in vivo*. We then investigated whether repeated motifs also occurred *in vivo* using 1.5- to 10-min intracellular recordings of the spontaneous (i.e., without visual stimulation) activity from neurons in primary visual cortex of anesthetized cats (11). Repeated motifs of synaptic activity were frequent *in vivo* (19 out of 21 neurons) (Fig. 1C) and occurred mostly in the absence of oscillations (96.5%), and significantly fewer repeats were found in shuffled traces (fig. S2Cii). Many motifs detected *in vivo* consisted of very large EPSPs (>10 mV), suggestive of synchronous input from several presynaptic neurons. The mean HRI (\pm SD) was 1.30 ± 0.64 ($n = 33,374$ motifs, 19 neurons). The average duration of a repeated motif was 1035 ± 357 ms. Patterns of EPSPs lasting up to 2 s repeated with millisecond precision, even after intermotif intervals of several minutes. *In vivo* motifs also occurred more than twice (14 out of 19 neurons) (Fig. 1Cii) and could also be found to occur simultaneously in paired intracellular recordings (6 out of 9 cell pairs; 110 ± 37 simultaneous motifs per cell pair).

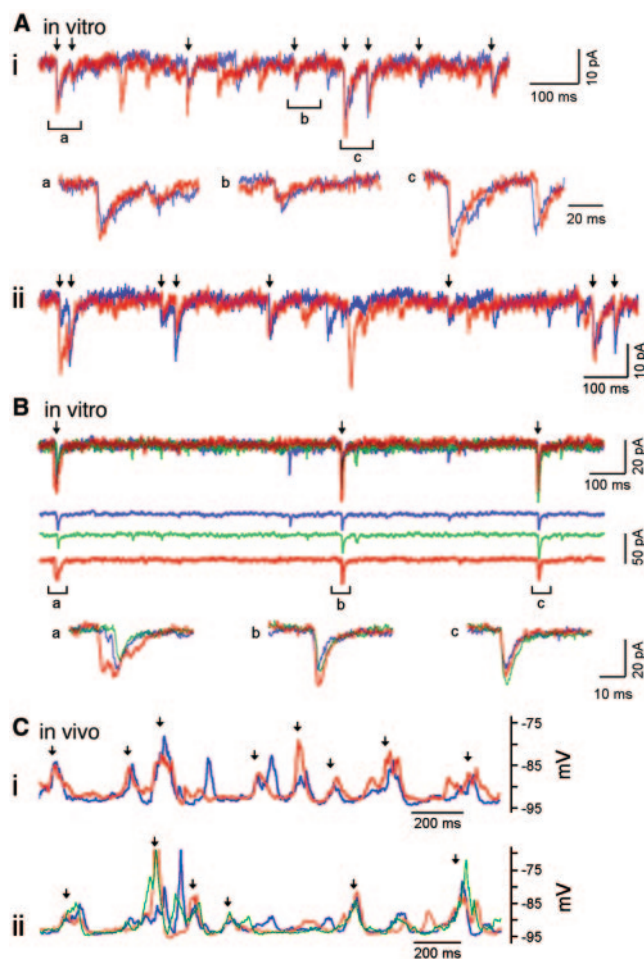
Repeated neuronal activation during motif repetition. We used calcium imaging to reconstruct, with single-cell resolution, the activity of neuronal populations (8, 12, 13)

¹Department of Biological Sciences, Columbia University, New York, NY 10027, USA. ²Department of Neurobiology and Physiology, Northwestern University, Evanston, IL 60208, USA.

*These authors contributed equally to this work.

†To whom correspondence should be addressed. E-mail: rmy5@columbia.edu

Fig. 1. Repeated motifs of spontaneous synaptic activity *in vitro* and *in vivo*. (A) Repeated motifs of intracellular activity from layer 5 pyramidal neurons in slices. Panels show segments (red) of the same voltage-clamp recording from the same cell repeating seconds or minutes after the initial occurrence (blue). Arrows indicate timings of repeated PSCs. (i) Upper trace: low-temporal resolution display of spontaneous activity of a neuron. Lower traces: higher resolution display of the repeated motif at indicated regions of the trace (a to c). (ii) Example of a longer motif. (B) Three repetitions of a motif. The top traces show the motifs superimposed on each other (blue, green, and red), the middle traces show these same traces individually, and the bottom traces show temporally magnified regions of the motifs (a to c). (C) Repeated sequences of intracellular current-clamp recordings *in vivo*. Two (i) and three (ii) repetitions of motifs are shown. Shuffle tests were performed on traces (i), a to c, yielding significantly fewer repeats (fig. S2, $P < 0.02$). In (i), the blue trace is shifted -2.75 mV; in (ii), the blue trace is shifted -1.58 mV, and the green $+0.79$ mV.



during the simultaneous occurrence of repetitions of an intracellular motif (Fig. 2). We loaded 97 brain slices from postnatal day 13 to 22 (P13 to P22) mice with calcium indicators and obtained 148 movies from primary visual and medial prefrontal cortex using confocal or two-photon microscopy. The indicator labeled virtually all superficial neurons as assessed by Nissl counterstaining (Fig. 2A). All slices displayed spontaneous calcium transients, which involved about 10% of cells during 120 s of imaging (fig. S3A). In intracellular recordings from imaged cells, spontaneous calcium transients were always synchronous with action potentials (Fig. 2B) ($n = 7$ cells) and were blocked by $1 \mu\text{M}$ tetrodotoxin or 2 mM Ni^{2+} ($n = 9$ slices). Most calcium transients were linked to action potentials generated during UP states (Fig. 2, B and C). Onset timing of action potentials could be reliably reconstructed by thresholding the first derivative of the optical traces (Fig. 2, D and E).

To explore the relation between the optically recorded sequences and the intracellular motifs, we performed intracellular recordings during slow-resolution (1 frame/s) two-photon imaging experiments. Neurons active during the first appearance of a motif were also active during its repetition (Fig. 3B) ($n = 10$ motifs; mean HRI = 1.1 ± 0.17). The mean number of optically detected neurons repeating during a motif was 3.6 ± 1.0 . The marked correlation between intracellular motifs and repeated sequences of network activity indicates that the repeated motifs are produced by the reactivation of the same circuits.

Fast imaging of spontaneous activity reveals repeating sequences. To investigate the dynamics of spontaneous activity with faster time resolution, we used confocal imaging (25 to 100 ms/frame). We created raster plots of the spontaneous activity produced by 445 to 1353 neurons (average 952.6 ± 31.3 imaged cells, $n = 57$ slices) and searched these plots with a template-matching algorithm for precisely repeating sequences of activation (7, 8). Such sequences were common, being present in 42 out of 58 movies (Fig. 3A) ($n = 3115$ sequences, average = 53.7 ± 10.3 sequences per movie, ranging from 0 to 341). Sequences involved 3 to 10 cells, lasted 2.9 ± 0.1 s (fig. S4), and repeated two to four times. To estimate the statistical significance of the occurrence of the sequences, we compared the incidence of sequences in real raster plots with surrogate raster plots obtained by three independent shuffling methods. In all types of surrogates, sequences appeared much less frequently than occurred in real data ($P \ll 0.001$) (Fig. 3, E to G). Similar results were obtained when different frames of jitter were allowed for template-matching (Fig. 3, E to

G). On average, $50.4 \pm 3.8\%$ of transients in single movies played a part in at least one sequence. For comparison, in intersignal intervals (ISI)-shuffled surrogates, at most 9.9% of transients were components of sequences. In addition, most transients simultaneously participated in different sequences; on average, individual transients were used in 1.91 ± 1.41 sequences, whereas they were used in only 0.12 ± 0.09 sequences in ISI-shuffled raster plots.

Timing and topography of repeating sequences. We further characterized the temporal and spatial structures of these repeated sequences. The timing jitter of calcium transients participating in sequences was independent of the sequence length (Fig. 3C), so the temporal precision of these sequences is preserved during their occurrence. To investigate whether these sequences persisted in time, we analyzed movies taken from the same slice for sev-

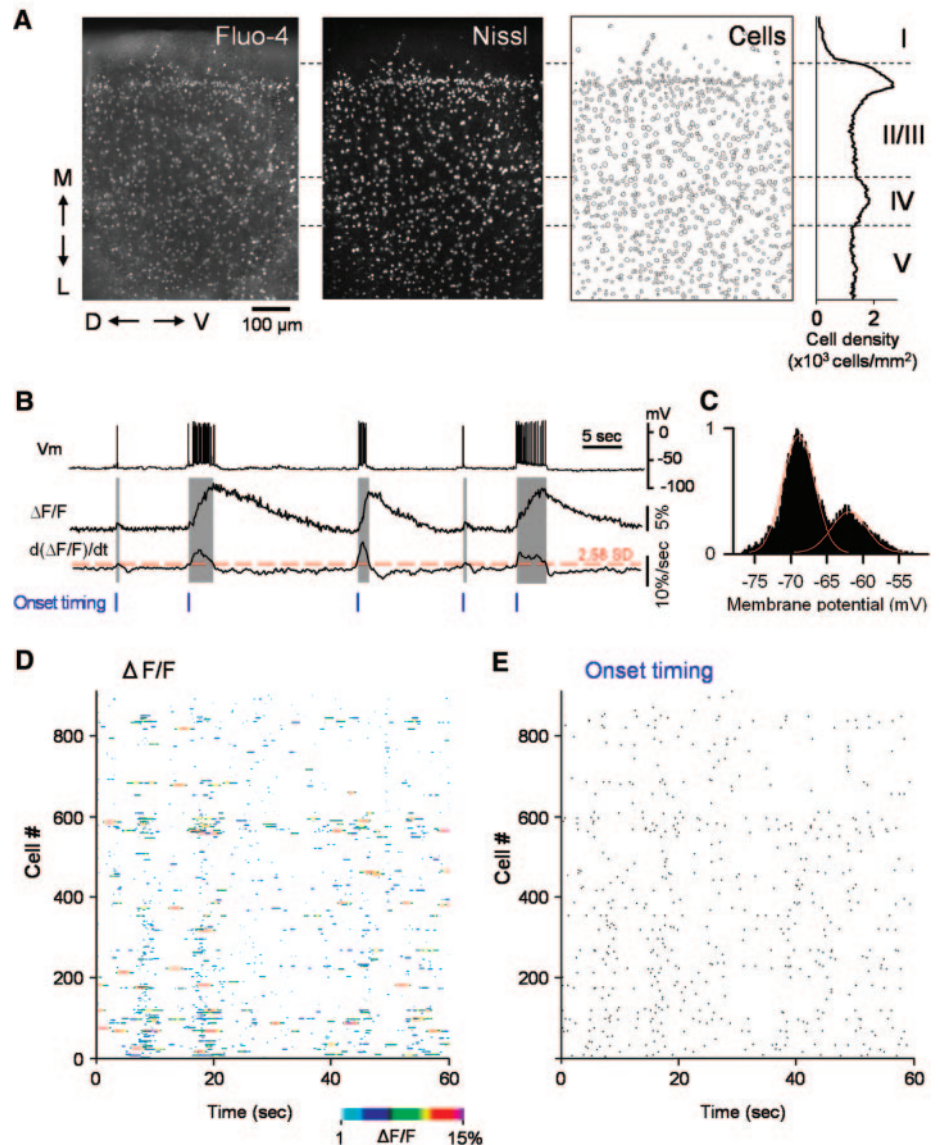


Fig. 2. Calcium imaging of spontaneous action potentials in large neuronal populations. (A) Confocal images of fluo-4 (left) and red Nissl (middle) and positions of the 866 automatically detected cells (right) of a slice of the medial prefrontal cortex. Layers were determined based on cell density. M, medial; L, lateral; D, dorsal; V, ventral. (B) Correlation between calcium transients and action potentials. Simultaneous current-clamp recording (top) and calcium imaging (middle). Onsets of spike timings (shaded areas) are detected as suprathreshold periods ($2.58 \times \text{SD}$ of noise, red) in the first derivative of the calcium signal. Most calcium transients are associated with UP states. (C) Bistable membrane potentials of a pyramidal cell. The plot was well fitted to a bimodal Gaussian distribution (red), indicative of DOWN and UP states of membrane potentials. (D) Pseudo-colored plot of calcium signals obtained from the slice in (A). Each row represents a single cell. (E) Raster-plot reconstruction of the onsets of spiking activity from (D). Out of the 866 cells, 137 cells (15.8%) showed spontaneous calcium transients.

eral hours. The subset of active cells dynamically drifted over tens of minutes (Fig. 3D and fig. S5); on average, $30.8 \pm 3.1\%$

of cells that were activated during a movie were reactivated in any subsequent movie, despite there being no prominent changes

in the total number of activated cells across movies (fig. S5A).

Sequences had specific topographic structures, in some cases involving only a particular layer or a vertical column of cells or cells located in a cluster (Fig. 4, A and B, and fig. S3B). Moreover, the spatial trajectory of the activation also precisely repeated and could follow the same direction with sequential steps. Therefore, repeating temporal patterns of activation, themselves statistically unlikely to emerge by chance, were associated with a structured spatial organization of the neurons that formed them.

Neuronal synchronization associated with the occurrence of repeated sequences.

One prediction of the “synfire” hypothesis is that repeating sequences should be specifically associated with synchronizations of the network (5). Consistent with this prediction, calcium transients were overwhelmingly produced by UP states (Fig. 2, B and C), which are reflections of circuit synchronization (13, 14). Also, time histograms of coactive cells demonstrated intermittent synchronization of spontaneous activity (Fig. 4C) (13). The synchronization appeared to be aperiodic, as assessed by Fourier analysis (fig. S6). To quantify synchronicity, we determined the *P* value of synchrony level as a function of time (Fig. 4C, red trace), defined as a probability that the same or higher level of coactivation could occur by chance in 1000 ISI-shuffled surrogates. In 52.1% of repeated sequences, the *P* value during the sequences fell below 0.05 ($n = 2983$ sequences), far in excess of what we found in ISI-shuffled data (13.6% of sequences with $P < 0.05$; $P \ll 0.001$, χ^2 test). Our analysis likely underestimates true synchronicity because we only image neurons in the plane of focus, which are a minority of the neurons present in the brain slice. Synchronization increased as a function of sequence repetition (Fig. 4D), suggesting that sequences were replayed with increasing synchrony.

Cortical songs: modular assemblies of repeated sequences.

When examining the temporal pattern of repeated sequences on larger time scales, we noticed that series of sequences could be repeated in the same sequential order (Fig. 4C). These supersequences, referred to here as “cortical songs,” were detected in 32 out of 54 movies. Each cortical song consisted of two to eight sequences (average 6.2 ± 0.1 , $n = 2636$ songs in 54 movies) and was repeated two or three times. The number of cortical songs found ranged from 0 to 321 per movie, averaging 48.8 ± 11.4 ($n = 54$ movies), far in excess of the number of songs that can emerge after shuffling of sequences (fig. S7). A sequence could par-

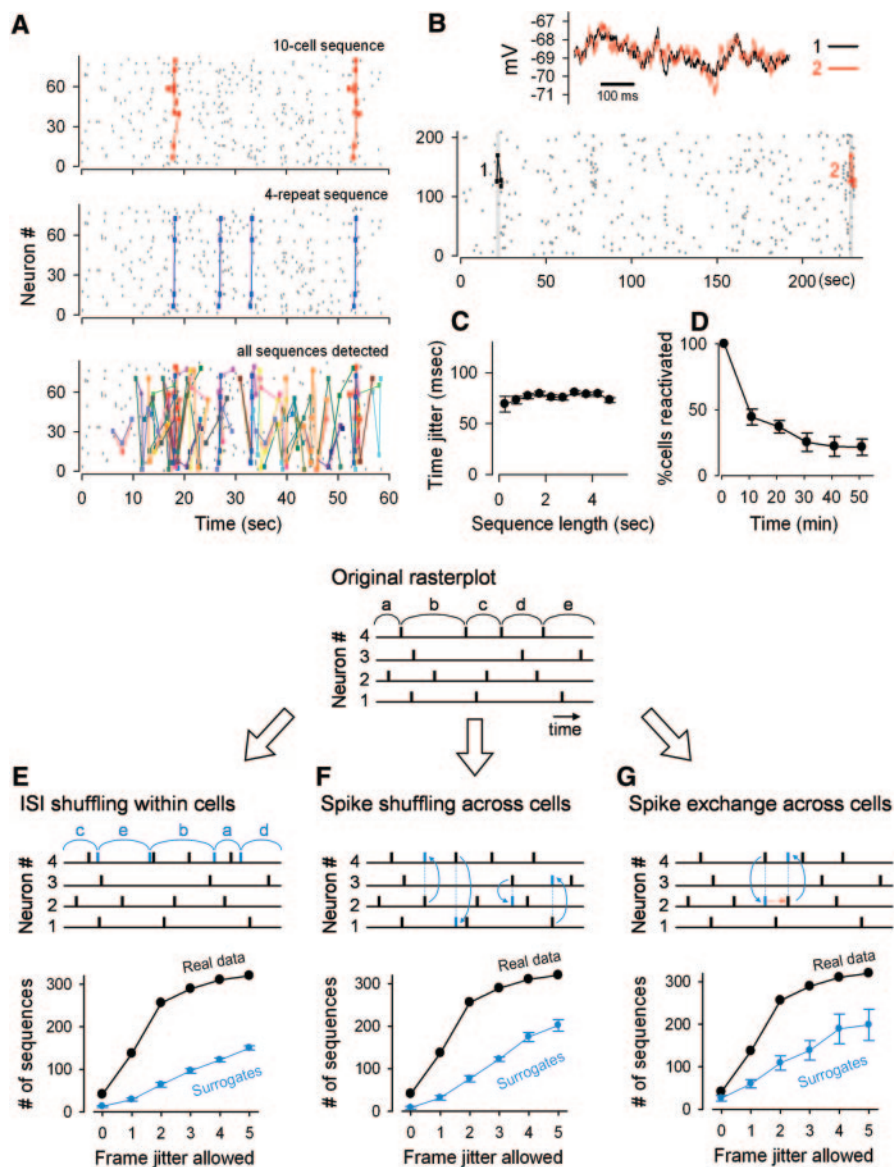


Fig. 3. Repeated motifs during sequential reactivation of identical cells. Properties of the repeated optical sequences. (A) Set of neurons with precise sequences of calcium transients (V1 slice). Ten cells (red) reactivated with exact timings between their transients (“sequence”) (top panel). In the same raster plot, a four-cell sequence (blue) is reactivated four times (middle panel). This four-cell sequence also acted as a part of the 10-cell sequence. Bottom panel shows all sequences detected in the same raster plot. (B) Simultaneous recording of intracellular motifs and repeated sequences. Raster plot displays a group of four cells activated in the same sequence during the time at which a motif and its repeat are detected simultaneously in the intracellular recording (gray, upper trace) of a layer 5 pyramidal cell. (C) The precision of the repetition is constant with the duration of the sequence. (D) Probability that cells active during a period from 0 to 2 min were reactivated in subsequent movies (means \pm SEM of six movies). (E to G) Spike sequences occur more frequently than expected by chance. Three independent methods of spike shuffling were used to examine how frequently sequences emerge by chance, as assessed by comparing the number of sequences in real spike trains (original raster plot) and their surrogates. Zero to five frames of jitter were allowed for repeated sequences. Data in Fig. 4A were analyzed (means \pm SD). (E) The intersignal intervals (ISI) were transposed at random within each cell in order to eliminate temporal correlation between the events. (F) Events were shuffled across cells while keeping their timings unchanged so as to preserve population modulation of event timings such as synchronization. (G) Spikes were exchanged between any pair of cells while maintaining their timings. The exchange procedures were repeated twice as many times as the number of spikes in the raster plot. In this randomization, event frequency within each cell and population modulation are both retained.

participate in more than one song; on average, single sequences were used in 3.7 ± 0.6 different songs ($n = 2983$ sequences). The numbers of sequences and songs detected in individual movies had a positive correlation (Fig. 4E).

The occurrence of the repeated sequences or songs was not correlated with the rate of activity (Fig. 4F), which indicates that cortical slices can generate repeated sequences, independent of the degree of network activity. In four out of six slices tested, the number of sequences and cortical songs fluctuated spontaneously without apparent changes in spike frequency.

Cortical songs were often repeated at faster time scales (Fig. 5, A and B). We quantified the temporal elasticity of the repetition with an orthogonal regression method, finding a biased distribution toward increasing compression during the course of a recording session (Fig. 5C) ($P < 0.01$) and that the precision in relative timing (as captured by the regression error) was more accurate than expected by chance (Fig. 5D). The temporal compression agrees with the increasing synchronization detected with increasing repetitions of a sequence (Fig. 4D). Also, the preservation of the precision of the songs is in accordance with the preservation of the jitter of individual sequences (Fig. 3C).

Modulation of cortical sequences and songs by NMDA and dopamine receptors.

Finally, we explored the synaptic mechanisms underlying the generation of cortical sequences and songs. It has been proposed that correlated network operation depends on *N*-methyl-D-aspartate (NMDA) receptor channel kinetics (15). In support of this proposal, the NMDA receptor antagonist APV (D,L-2-amino-5-phosphonovaleic acid) depressed the occurrence of cortical sequences and songs without affecting the activity rate (fig S8). We also compared the spatiotemporal coordination of spiking activity before and after application of dopamine, because dopamine also appears to be involved in persistent neuronal activity (16). Although we found no apparent effect of dopamine on the incidence of spiking activity, dopamine suppressed the occurrence of cortical sequences and songs (fig S9). This effect was specifically inhibited by SCH23390, a D1 receptor antagonist, and mimicked by SKF38393, a D1 agonist. Slight, but significant, increases in sequences and songs were induced by SCH23390, suggesting that endogenous dopamine is working under resting conditions. Aberrant functions of D1 receptors and NMDA receptors, both of which have been implicated in the pathophysiology of schizophrenia (17), thus induce functional disconnection of neuronal modules.

Discussion. Intracellular recordings and imaging experiments reveal the widespread existence of repeated dynamics in the spontaneous activity of neocortical circuits in vitro and in vivo. The ability to reconstruct

the activity of a large (>1000) population of neurons, and the increased statistical power of correlating intracellular records rather than spikes, have facilitated the detection of these dynamics. These repeated

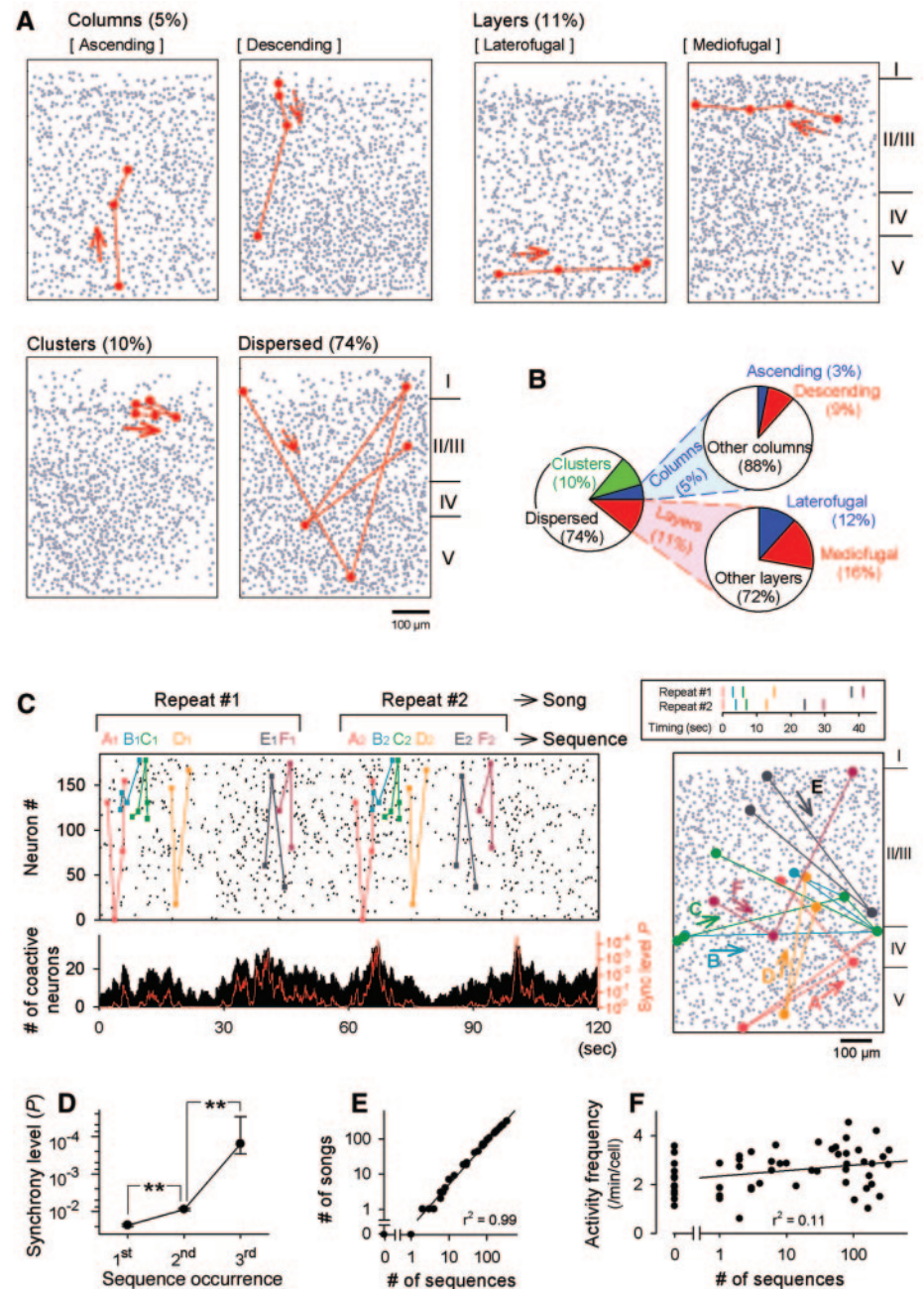


Fig. 4. Anatomical structure of the sequences. High-order sequences (cortical songs). (A) Representative maps of six types of spatial arrangement of neurons involved in sequences. Neurons are sequentially activated, as indicated by the arrows. (B) Frequency of each spatial pattern ($n = 2983$ sequences from 54 movies; medial prefrontal cortex). (C) (Left panels) Representative cortical song. A total of 181 of 1197 cells showed spontaneous activity (left top panel). Subsets of neurons displayed temporally precise sequences of activity (sequences: A1 to F2). The sequences were repeated in the same order (cortical song: A>B>C>D). Bottom histogram represents the number of cells active at each frame of the movie. The red line expresses the *P* value of synchronization, defined by random ISI shuffling (13). (Right panel) Onset timings of songs (top) and locations of cells (bottom). (D) Synchrony levels increase as a function of sequence occurrence. $**P < 0.01$; Bonferroni/Dunn test (means \pm SEM of 2983 sequences, 54 movies). (E) Correlation between the number of sequences and songs. Each dot represents a single movie. The line represents best linear fit. (F) Lack of correlation between the number of sequences and rate of activity.

patterns are robust; not only do they occur more frequently than expected by chance, but they can happen at the same time in two neurons, occur simultaneously in intracellular and optical recordings, are correlated with intracellular UP state depolarization and with network synchronizations, involve circuits with structured topographies, form modular patterns with compressing timing, and are blocked by D1 activation receptors. Our results demonstrate that the apparently stochastic cortical synapses can work with high reliability to produce stereotypical dynamics that are reduced in dimensional space. Our data agree with the prediction that cortical activity flows through chains of synchronized neurons (synfire chains), which are reactivated with high temporal precision. Moreover, we describe a higher order grammar (18), by which these chains themselves can be modules of larger tem-

poral structures (cortical songs), defined by their sequential order of activation, and which can last for minutes. These songs resemble spiking correlates of sequential behavior, like bird songs (19, 20) or spatial navigation (21), and have compressing dynamics, as if the circuit was replaying and modifying previously learned sequences (21–23). The mechanisms that generate and propagate synfire chains and cortical songs must be intrinsic to the cortical circuit, because they are preserved in slices, and might reflect the faithful reactivation of specific circuits (24), mediated by stereotypical synaptic dynamics (25, 26) and driven by pacemaker cells (8, 27). Because the activity drifts with time, it is also possible that short-lived patterns, perhaps reflecting ongoing circuit memory, are generated de novo (6, 28). Regardless of the mechanism, the repeated dynamics that we

observed involve UP states, and the progression of activity is therefore briefly settling into preferred states of persistent activity, so our data link synfire chains with attractor neural networks (6, 13, 29). We conclude that the neocortex can spontaneously generate precisely reverberating temporal patterns of activation (5, 30), dynamic ensembles that could represent endogenous building blocks of cortical function (31, 32).

References and Notes

1. V. B. Mountcastle, *Perceptual Neuroscience: The Cerebral Cortex* (Harvard Univ. Press, Cambridge, MA, 1998).
2. H. Markram, M. Tsodyks, *Nature* **382**, 807 (1996).
3. L. F. Abbott et al., *Science* **275**, 220 (1997).
4. C. Stevens, *Curr. Biol.* **4**, 268 (1994).
5. M. Abeles, *Corticonics* (Cambridge Univ. Press, Cambridge, 1991).
6. M. Diesmann, M. O. Gewaltig, A. Aertsen, *Nature* **402**, 529 (1999).
7. M. Abeles et al., *J. Neurophysiol.* **70**, 1629 (1993).
8. B. Q. Mao et al., *Neuron* **32**, 883 (2001).
9. M. W. Oram et al., *J. Neurophysiol.* **81**, 3021 (1999).
10. Materials and methods are available as supporting material on Science Online.
11. I. Lampl, I. Reichova, D. Ferster, *Neuron* **22**, 361 (1999).
12. R. Yuste, L. C. Katz, *Neuron* **6**, 333 (1991).
13. R. Cossart, D. Aronov, R. Yuste, *Nature* **423**, 283 (2003).
14. Y. Shu, A. Hasenstaub, D. A. McCormick, *Nature* **423**, 288 (2003).
15. X. J. Wang, *Trends Neurosci.* **24**, 455 (2001).
16. P. S. Goldman-Rakic, *Neuron* **14**, 477 (1995).
17. W. Franke, J. Lerma, M. Laruelle, *Neuron* **39**, 205 (2003).
18. E. Bienenstock, *Neural Comput.* **6**, 179 (1995).
19. F. Nottebohm et al., *Philos. Trans. R. Soc. London B Biol. Sci.* **329**, 115 (1990).
20. R. H. Hahnloser, A. A. Kozhevnikov, M. S. Fee, *Nature* **419**, 65 (2002).
21. K. Louie, M. Wilson, *Neuron* **29**, 145 (2001).
22. W. L. Skaggs, B. L. McNaughton, *Science* **271**, 1870 (1996).
23. Z. Nadasdy, H. Hirase, A. Czurko, J. Csicsvari, G. Buzsaki, *J. Neurosci.* **19**, 9497 (1999).
24. J. Kozloski, F. Hamzei-Sichani, R. Yuste, *Science* **293**, 868 (2001).
25. G. Silberberg, C. Wu, H. Markram, *J. Physiol.* **556.1**, 19 (2004).
26. D. V. Buonomano, *Proc. Natl. Acad. Sci. U.S.A.* **100**, 4897 (2003).
27. R. R. Llinás, *Science* **242**, 1654 (1988).
28. W. Maass, T. Natschlagler, H. Markram, *Neural Comput.* **14**, 2531 (2003).
29. J. J. Hopfield, *Proc. Natl. Acad. Sci. U.S.A.* **79**, 2554 (1982).
30. R. Lorente de Nó, *J. Neurophysiol.* **1**, 207 (1938).
31. A. Grinvald et al., *Biopolymers* **68**, 422 (2003).
32. R. Llinás, *I of the Vortex: From Neurons to Self* (MIT Press, Cambridge, MA, 2002).
33. We thank D. Anastassiou for access to the Regatta supercomputer, W. Maass and members of our laboratory for comments, and the late P. Goldman-Rakic for suggestions and encouragement. Supported by the National Eye Institute, National Institute of Neurological Disorders and Stroke, University of Tokyo, and the New York State Office of Science, Technology and Academic Research (NYSTAR).

Supporting Online Material

www.sciencemag.org/cgi/content/full/304/5670/559/DC1

Materials and Methods

Figs. S1 to S9

References

Movies S1 and S2

31 October 2003; accepted 18 February 2004

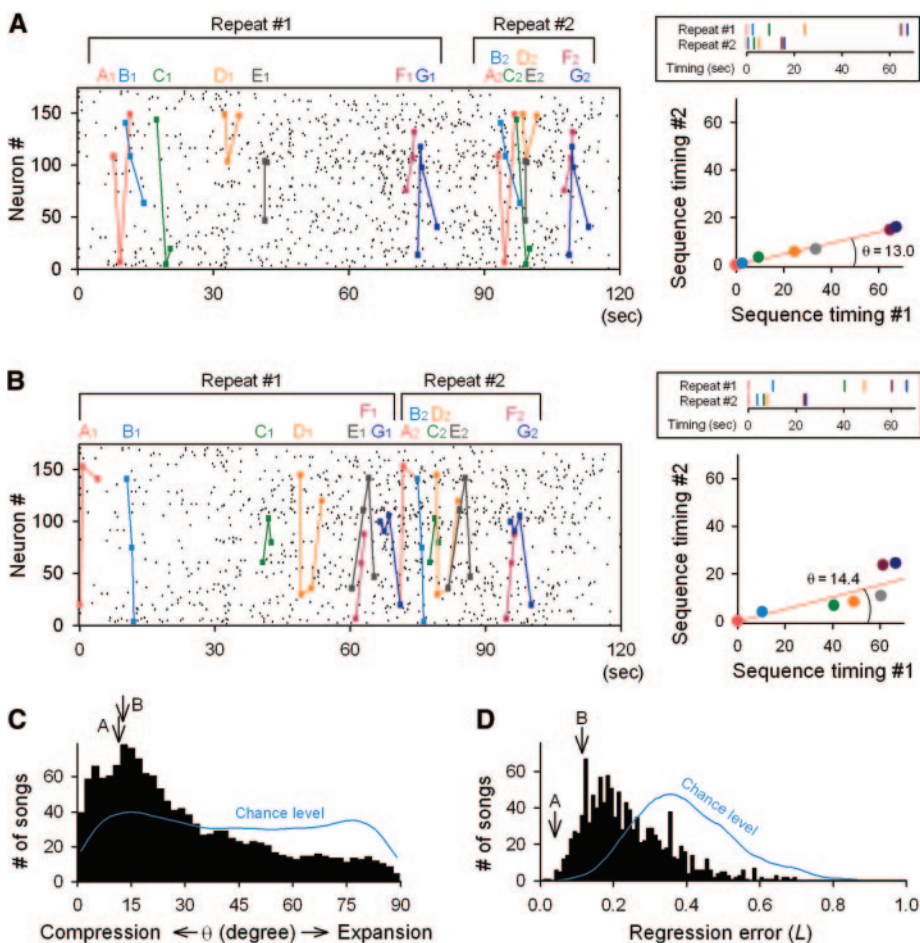


Fig. 5. Temporal compression of cortical songs. (A and B) Representative songs repeating at faster time scales, both found in the same raster plot. Right top panel indicates the onset timings of the sequences in each song. The right bottom scatter plots show regression analyses for timing correlations of the first song occurrence versus the second recurrence. (C) Asymmetric distribution of θ (average = $29.2^\circ \pm 0.6^\circ$; mean \pm SEM of 2636 songs, 54 movies). The distribution of 22,824 surrogate songs obtained for shuffled sequences (fig. S7) is shown as a chance level (blue). The values of the songs shown in the (A) and (B) are indicated by the arrows. (D) The distribution of regression error (L) after the pseudo-rotation coordinate transformation (10). The mean L values in the real data were significantly lower than expected by chance ($P < 0.001$; Bonferroni/Dunn test).

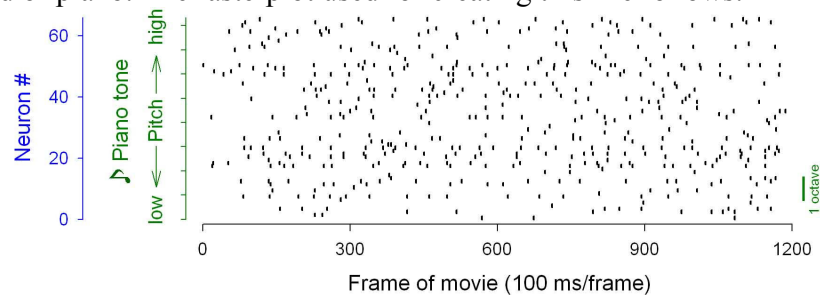
Supporting Online Material

1. Original Data

1.1 Text file included is the original data of Fig. 1A. Recorded from a layer 5 pyramidal neuron in mouse primary visual cortex in vitro. File has data sampled at 1kHz instead of the 10 kHz in the figure. Original recording was 8 minutes long, whereas this file contains 150 seconds of recording, centered around the motif and repeat of interest. The motif starts at 23,935 ms. The repeat starts at 148,178 ms. The length of the motif and repeat is 985 msec. Each point in this text file represents a pA value with a time width of 1 msec.

1.2 Movie file (avi) is the confocal imaging data used as a part of Fig. 5A-C. Because the original movie is nearly 1 Gbytes, it was cropped in space and time, converted from a 16-bit to 8-bit scale, and compressed by lowering the image quality.

1.3 Sound file (mov) is an acoustic representation of cortical activity. Every neuron was assigned a pitch of the sound of piano. The rasterplot used for creating this file follows.



2. Materials and Methods

2.1 Electrophysiology and imaging:

PND 13-22 C57Bl/6 mice were anaesthetized and transverse 350 μm coronal slices of primary visual and medial prefrontal cortices were cut on a vibratome in modified ACSF that included 0.5 mM CaCl_2 , 7 mM MgSO_4 , and 0.5 mM ascorbic acid, in which NaCl was replaced by an equimolar concentration of sucrose. Slices were transferred to warm (37°C), oxygenated, ACSF (1.5 mM MgSO_4 , 2 mM CaCl_2), and allowed to equilibrate to room temperature. Whole-cell recordings from layer 5 pyramidal cells were performed using 6-9 M Ω pipettes, filled with (mM): 130 K-methylsulfonate, 11 biocytin, 10 KCl, 10 HEPES, 5 NaCl, 2.5 Mg-ATP, 0.3 Na-GTP. Recordings were made with an Axopatch 200B and a BVC-700 amplifier and digitized with an A/D board using Igor. Between 4 to 8 minutes of spontaneous activity was recorded in conventional ACSF (1 mM MgSO_4 , 2 mM CaCl_2 , 3 mM KCl, 34°C). Recordings were obtained in voltage clamp but similar results were found in current clamp.

In vivo recordings were obtained from paralyzed, barbiturate-anesthetized, adult cats (S1). Intracellular records were obtained with sharp glass micropipettes filled with 2M potassium acetate. Two electrodes were placed on the cortical surface with their tips less than 500 μm apart and angled approximately $10\text{--}15^\circ$ to the vertical axis so that they would approach each other as they were

advanced into the cortex. The exposed cortex was then covered with warm agar (3% in saline) to reduce respiratory and cardiovascular movements and prevent the cortex from drying. Membrane potentials were recorded with an Axoclamp-2A amplifier in bridge mode. Membrane potentials were low-pass filtered at 10 kHz prior to digitization at 20 kHz.

Confocal imaging was performed with a spinning disk confocal microscope. For Fig. 3B data, two-photon imaging was carried out with a custom-made two-photon microscope (S2) with a Ti:sapphire laser providing 130 fs pulses at 75 MHz, pumped by a solid-state source. Frames were acquired at 25-100 msec (confocal) or 1sec/frame (two-photon). Fluo-4 was used for confocal imaging and fura-2 for two-photon imaging. For fluo-4 indicator loading, a slice was exposed to 3 μ l of 0.1% Fluo-4-AM, 49.9% NeuroTraceTM 530/615 and 50% DMSO in 2 ml ACSF in the dark at 37°C for 20 min. For Fura2-AM-loading, slices were incubated in a small vial containing 2.5 ml oxygenated ACSF with 25 μ l of 1mM Fura-2-AM solution (in 100% DMSO) for 20–30 min. Slices were incubated in the dark at 35–37°C (S3). Experiments were performed at 37°C with ACSF (in mM: 123 NaCl, 3 KCl, 26 NaHCO₃, 1 NaH₂PO₄, 2 CaCl₂, 1.5 MgSO₄ and 10 dextrose). Drugs were applied by bath with addition of 100 μ M ascorbic acid. Images were collected on an Olympus BX50WI microscope equipped with an UltraView spinning disk confocal head with a 10X, 0.3 NA objective and captured with an Orca ER camera and a Imaging Suite software. Time-lapse series were acquired and saved as 16-bit tiff files. To minimize photodamage and photobleaching, we restricted confocal imaging to a period of 120 sec

2.2 Analysis of intracellular motifs:

Repeats of intracellular spontaneous activity (see supplementary files for representative examples) were detected and quantified as follows (Fig. S1): Voltage or current recordings were decimated to 1 point per ms and, using an supercomputer (IBM p690 Regatta) and custom MatLab and Igor routines, all 1 second long segments were compared against each other at 250 ms intervals. Each comparison was made by computing a covariance function (S4):

$$h(\tau) = \frac{\sum_{t=-T}^T (x_t - \bar{x})(y_{t+\tau} - \bar{y})}{\sqrt{\sum_{t=-T}^T (x_t - \bar{x})^2 \sum_{t=-T}^T (y_t - \bar{y})^2}}$$

Here, x and y are amplitudes from the respective motif and its potential repeat, and 2T+1 are the number of samples in each motif at 1 points per ms. As jumps of 250 ms are unlikely to find the regions of precise overlap, the program realigned the traces according to the difference between the peak value of the covariance function and the zeroth lag of function and then recomputed the function, provided that the peak value was initially within 250 ms of the zeroth lag. The value at the zeroth lag (h(0)) was then recorded. The highest values for each 1 second interval and those passing a set threshold (0.45) were collected for each recording and formed our low resolution similarity index (LRI). As the voltage clamp recording is composed of distinct fast signals, we further devised a method of analyzing these recordings that is sensitive to this (Fig. S1). Taking the results from the LRI, a total of 2 seconds encompassing those intervals were then analyzed in a similar manner but with 20 ms epochs and an amplitude normalization:

$$T = h_{20}(0) \cdot \left(1 - \frac{|m-r|}{|m|+|r|} \right)$$

Here, m is the particular 20 ms epoch of a trace, normalized to zero (a vector of 20 numbers (pA), with a mean of 0), r is the corresponding vector in the potential repeat of the motif, and $h_{20}(0)$ is the zeroth lag of the covariance function comparing the 20 ms segments, m and r . The 20 ms epochs that exceeded a set threshold (0.55) were saved (T values) for each 2 second segment. Motifs were defined by waveforms containing a cluster of 20 ms epochs. The total width of a motif was therefore limited to 2 seconds by this analysis and its width was measured from the first to the last 20 ms epoch of the cluster. We searched for repeats ranging from 100 ms to 2 sec. A final table of the motifs found in a recording included only those with a cluster containing a minimum of three 20 ms epochs and a total minimum 100 ms total duration. The final high-resolution index (HRI) of a motif was computed by the sum of all T values multiplied by the mean of all T values normalized by the difference in amplitudes of the motif and its repeat:

$$\text{HRI} = \frac{\left(\sum_{i=1}^n T_i \right)^2}{n} \cdot \frac{\sqrt{\text{std}(\text{motif}) \cdot \text{std}(\text{repeat})}}{|\text{motif} - \text{repeat}|}$$

Here, $\text{std}(\text{motif})$ is the standard deviation of the motif, and n is the number of T values found within the motif. Both motif and repeat are normalized to zero before HRI is computed. The HRI was developed empirically and appeared to produce the results with fewest apparent false positives and false negatives by visual inspection, as compared to the LRI. A P-value was derived for each repeat and motif, based on a correlation coefficient derived from $h(0)$ of the motif and repeat (Matlab, `corrcoeff` function), and any repeat with $P > 0.01$ was discarded. Finally, the HRI is not considered an absolute scale of the fidelity of a repeat; rather, it is a useful index for ranking these repeats and quickly finding the most striking examples. This test may be more demanding than would be required to find all motifs, since there is a penalty for differences in amplitudes of the synaptic events, and the amplitude of a current from a particular synapse usually varies from one activation to the next.

A small subset of these motifs found with HRI appeared oscillatory, and we devised a method to test whether the motif was detected because of an oscillation: a covariance function was calculated between the motif and repeat (as shown above, but in this case for the full length of the motif), and the largest peak outside of -20 to +20 ms of the zeroth lag and within 1/2 of the width of the motif was detected. The motif and repeat were then shifted +/- one period of the potential oscillation, according to this detected peak location, and the shifted traces were analyzed with the normal HRI procedure. If the shifted traces passed the minimum thresholds for the HRI, then the motif was considered oscillatory and not considered significant.

To test whether motif repetitions *in vitro* or *in vivo* occurred by chance, we performed two statistical tests (Fig. S2). First, with a shuffle test, we created fifty randomized waveforms from the data in which the EPSC or EPSPs shapes were exactly preserved as was the temporal order of these events, but the time intervals between these events were randomly shuffled. A shuffled trace created in this manner was therefore identical to an original trace in its statistical properties. For all cells, the original traces yielded more repeats than any shuffled trace (the best shuffled trace from each experiment had on average 14 ± 5.3 % fewer motifs than the original trace, 50 shuffles each, $p = 0.02$, 5 cells), indicating that chance alone was not the cause of the precise repetitions. In a second test, we asked whether repetitions could be found when comparing traces from one neuron to those from another cell from a different animal. This test therefore did not involve shuffling the data. In the slice data, we restricted this analysis only to cells of the same kind (large layer 5 pyramidal neurons) to help ensure a similar distribution of PSC kinetics. In this analysis we found that HRIs

were significantly higher from individual cells than from across cells from different animals (1.12 ± 0.10 vs. 0.83 ± 0.06 , mean of means from each cell or cell pair, $p < 0.02$, Wilcoxon rank sum test, $n = 20$ neurons). Furthermore, all HRIs from individual cells were significantly higher than those from across cells from different animals (1.24 ± 0.01 vs. 1.07 ± 0.01 , $p < 0.001$, Wilcoxon rank sum test, $n = 16271$ vs. 5214 detected motifs, respectively). We concluded that motif repetitions did not occur by chance. For the shuffle test, PSP/Cs were detected by computing a covariance function of a mean PSP/C risetime waveform against the entire spontaneous recording: this produced a waveform whose peaks marked the onset of PSP/Cs, and peaks passing a set threshold were taken as the start times of PSP/Cs. These onset times were also used to compute the jitter between PSCs in the motif-repeat pairs (see accuracy of onset detection in Fig. 1). All intervals less than 20 ms were cut from the array. Using this array of start times, we extracted 20 ms segments of the spontaneous recording and placed these extractions on a baseline at 0 mV to form a trace that represented the extracted PSP/Cs of the original recording. The distribution of intervals between these extracted PSP/Cs were randomly shuffled, and 50 shuffled traces were composed from these shuffled distributions for each unshuffled trace. A distribution of LRIs were computed for shuffled traces and compared to the LRIs of unshuffled traces. Due to the intensive computing time required for this procedure, it was only performed on a subset of the data (4 voltage-clamped cells in vitro, one 10 minute-long current clamp cell, in vivo and 3 voltage-clamped cells in vitro recorded in tetrodotoxin), and the HRI was not computed for the same reason. Procedures for computing the HRI and shuffle test were the same for current clamp recordings except that 100 ms increments instead of 20 ms increments were used in order to better match the longer kinetics of PSPs versus PSCs.

2.3 Analysis of imaging data:

Calcium signals of neurons were extracted from movies by using custom-written software in ImageJ (National Institutes of Health) and Matlab (MathWorks) (S3). Subsequent analyses were performed with Microsoft Visual Basic routines. Neurons were automatically identified in Nissl images to create cell contours, within which the fluorescence intensity was measured. For each cell, we defined the fluorescence change as $\Delta F/F = (F1-F0) / F0$, where F1 is fluorescence at any time point, and F0 is the baseline fluorescence averaged across the whole movie. To detect optical events, the first derivative of each trace was calculated by sliding a 1-sec cursor after smoothing the trace with a 300-msec-window Hamming filter, and suprathreshold changes were detected as calcium transients (S5). The threshold was set to $2.58 \times SD$ ($P < 0.01$) of noises, which were calculated from 5,892 cells in the presence of 1 μM tetrodotoxin or 2 mM Ni^{2+} . We then scrutinized all detected events by comparing original traces and manually rejected noises if they were erroneously detected. Noise events were easily distinguishable from spike-relevant events by eye because spikes were followed by slower calcium decays over hundreds of milliseconds (S6).

The topographic structures of sequences were identified and classified using Monte Carlo simulations (S3). First, we determined whether the arrangement of cells involved in a sequence could be classified into one of three spatial patterns (clusters, columns or layers). We characterized each pattern of coactive cells by three measurements: the average distance between cell locations and their centroid, the average length of the projections of these distances in the direction parallel to the pia, and the average length of the projections in the direction perpendicular to the pia. For each pattern, we created 1,000 surrogate arrangements of cells using Monte Carlo simulations, choosing the same number of cells at random from the slice each time. All three measurements were made for

each of the surrogate patterns, and the significance of the spatial arrangement was determined by directly comparing the resulting distributions with the original measurements. If the distance projections were significantly small ($P < 0.05$) only in the direction parallel or perpendicular to the pia, the pattern was classified as a column or a layer, respectively. If the unprojected distances were significantly small, the pattern was classified as a cluster. If a sequence is classified into a column pattern, we next sought to determine whether the sequential activation of the cells in the sequence could be classified into an ascending or descending pattern. Similarly, if a sequence is classified into a layer pattern, we examined whether it could be classified into a laterofugal or mediofugal pattern. In this subclassification, we introduced the following formula as an index;

$$C = \sum_{i=1}^{n-1} \frac{a'_i \cdot e}{\sqrt{a'_i \cdot a_i}}$$

where a_i is a spatial vector from cell_{*i*} to cell_{*i+1*} in a sequence (sequential n cells), and e is an unit vector perpendicular (columns) or parallel (layers) to the pia. For each pattern, we again created 1,000 surrogate arrangements of cells and determined the 5% significant level of the value C for selection of structured sequences.

To determine the significance level of activity synchronization, we created surrogate rasterplots, in which ISI was reshuffled at random within cells with keeping event durations constant, and collapsed it into the time histograms of coactive cells. We calculated the probability that any given number of cells was coactive. We repeated the reshuffling 1,000 times to estimate the P-value of the statistic.

We used a template-matching algorithm for global search for sequences. To speed up this process, we first selected cells that showed more than one calcium transient. After determining the reference calcium events of the reference cell (*cell*_{*1*}), we designated a vector consisting of a set of cells and relative timings of their calcium events as follows: (*cell*_{*2*}, ..., *cell*_{*N*}, t_2, t_3, \dots, t_N), where t_i denotes the delay of the event of cell_{*i*} after the reference event. t_i was limited to less than 5 sec of time window. This vector was considered as a template and slid along the successive events of *cell*_{*1*} throughout the recording session. If more than two elements were identical between any template pairs, we regarded the matched elements as a sequence. Each mismatch spike configuration was used as another template in a subsequent scan. Thus, every event was considered as a part of a template sequence, and each template occurred at least once. Unless otherwise specified, one frame jitter was allowed because the power of sequence detection (signal-to-noise) was maximal at this jitter (S1). As a result, the entire parallel train was exhaustively searched for repetition of all possible sequences. The same method was further applied to the onset timing of sequences to detect songs, in which case, however, we focused only on the sequential orders of sequences, ignoring their timings. We regarded any repeated sequence consisting of more than one sequence as a cortical song.

To quantify the compression/expansion states and temporal precision of songs, we used an orthogonal regression method by the bivariate principal component analysis, in which the onset timings of the sequences comprising a song were fitted to the direct proportional line $t' = t \tan\theta$ in the space of the first song occurrence (t) vs. the second recurrence (t') (the right-lower panels in Fig. 5A-B). Onset timings of N sequences comprising a song can be expressed as vectors, i.e., (t_1, t_2, \dots, t_{N-1}) for the first occurrence and ($t'_1, t'_2, \dots, t'_{N-1}$) for the second recurrence, where t_i or t'_i denotes the delay of sequence_{*i+1*} from the first sequence_{*1*}. For pairwise comparison, the vectors were fitted to the direct proportional line $t' = t \tan\theta$, where θ is defined so as to minimize the residual S :

$$S = \sum_i^{n-1} (t'_i \cos \theta - t_i \sin \theta)^2$$

In this regression analysis, therefore, the θ -value represents the compression/expansion state of the song; if θ is less than 45° , the song is temporally compressing, and if θ is more than 45° , it is expanding. The regression error reflects the precision in the relative timings of the sequences; the higher precision gives the lower regression error. Because the simple regression error was critically influenced by θ , we performed a pseudo-rotation coordinate transformation in the space of (t_i, t'_i) , in which θ was transformed to 45° with keeping the ratio of $\tan \theta : t'_i / t_i$ constant and maintaining the x-y axis direction. As a result, the new coordinate of (t_i, t'_i) is given as

$$\left(\frac{t_i \sin \theta \sqrt{t_i^2 + t_i'^2}}{\sqrt{t_i^2 \sin^2 \theta + t_i'^2 \cos^2 \theta}}, \frac{t'_i \sqrt{t_i^2 + t_i'^2}}{\sqrt{t_i^2 \sin^2 \theta + t_i'^2 \cos^2 \theta}} \right)$$

Now we defined the modified regression error L as follows.

$$L = \frac{1}{n-1} \sum_i^{n-1} \left| \frac{t'_i \cos \theta - t_i \sin \theta}{t'_i \cos \theta + t_i \sin \theta} \right|$$

Thus, L can range from 0 to 1.

We report the mean \pm standard deviation in all measurements, unless otherwise stated.

3. References in the supporting material

- S1. J. Anderson, M. Carandini, D. Ferster, *J. Neurophysiol.* 84, 909-926 (2000).
- S2. V. Nikolenko, B. Nemet, R. Yuste, *Methods* 30, 3-5. (2003).
- S3. R. Cossart, D. Aronov, R. Yuste, *Nature* 423, 283-289. (2003).
- S4. I. Lampl, I. Reichova, D. Ferster, *Neuron* 22, 361-74. (1999).
- S5. D Smetters, A Majewska, R Yuste. *Methods* 18, 215-21 (1999).
- S6. B. Q. Mao, et al., *Neuron* 32, 883-98. (2001).

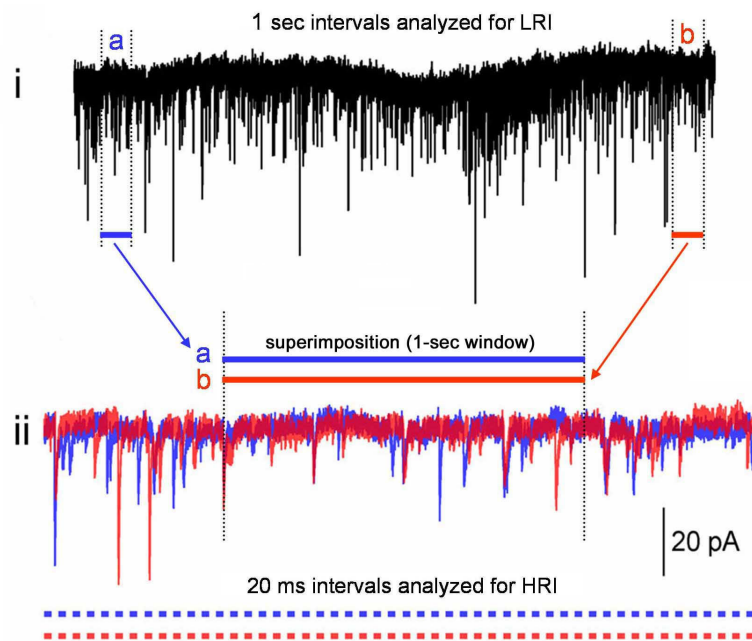


Fig. S1. Detection of repeated intracellular motifs. Approximately 19 seconds of a voltage clamp recording is displayed. Two 1-second regions are highlighted (blue (a) and red (b) trace) that have passed threshold for the LRI (i). These two regions are then analyzed again, using the HRI where every 20-msec region they have in common are compared (ii).

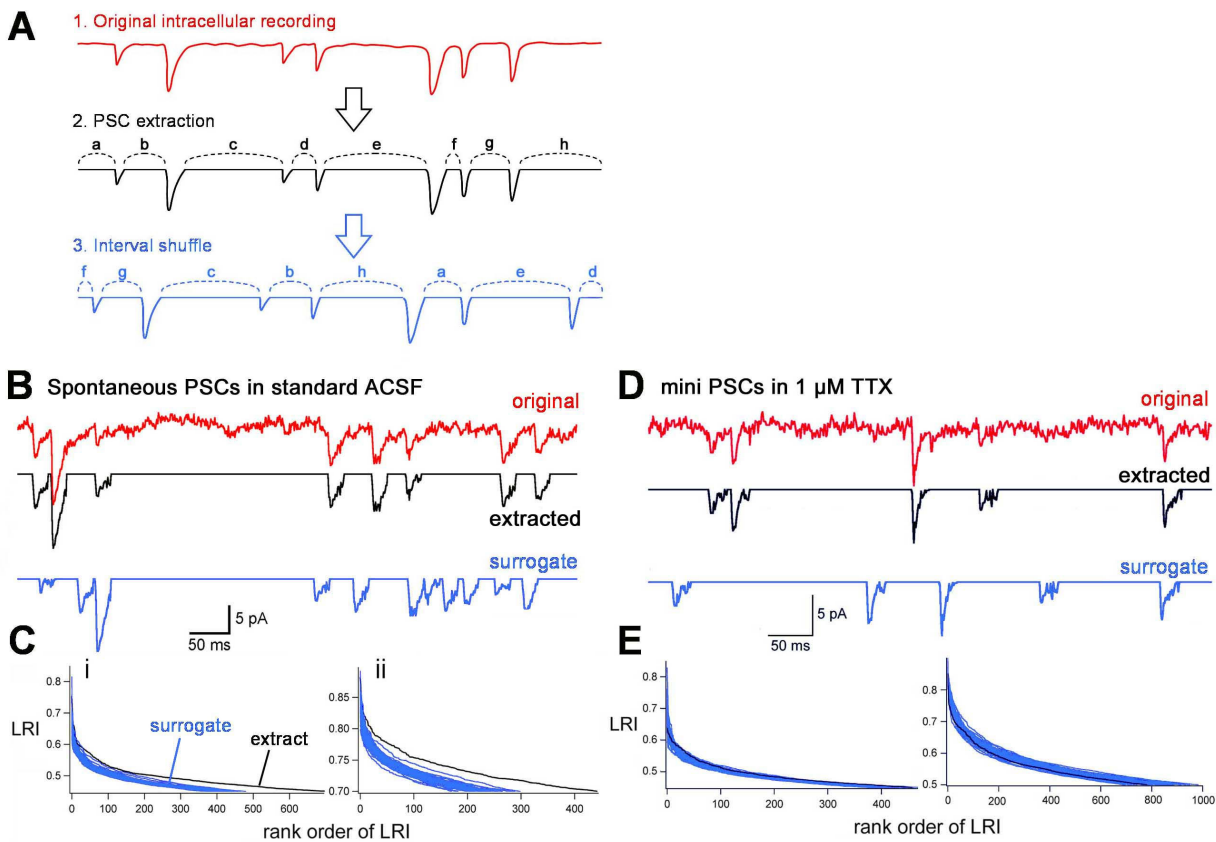


Fig. S2. Repeated motifs do not occur by chance. (A) Schematic drawing of the inter-signal interval (ISI) shuffling of intracellular traces. PSCs (2) were extracted from an original trace (1), and the time intervals between these events were randomly shuffled with the temporal order of these events exactly preserved (3). (B) The red trace shows the original in vitro voltage clamp trace (same cell as Fig 1A). The superimposed black trace is the extracted PSPs. Note that most PSCs are detected, but some are not completely extracted in order to avoid overlaps of PSCs in shuffled traces. The blue trace is one of 50 shuffled traces. Note the same order of events, and the difference in intervals. (C) (i) These shuffled traces were fed into the same program used to compute LRIs for real data. The distribution in black is composed of the rank ordered LRIs from the real data (extracted trace, 1A), while the blue is the rank-ordered LRIs from the shuffled traces. The real data produces a distribution of LRIs clearly distinguished from the shuffled traces. (ii) The same analysis was applied to a 10 minute current clamp recording in vivo (same recording yielding traces in Fig. 1C). The real data yielded more motifs than any shuffled trace ($p = 0.02$). (D, E) Same analysis repeated for miniature PSCs recorded in 1 μ M tetrodotoxin. Two examples out of three recordings are shown in E. In all tetrodotoxin recordings, several shuffle traces that had more motifs than the real data.

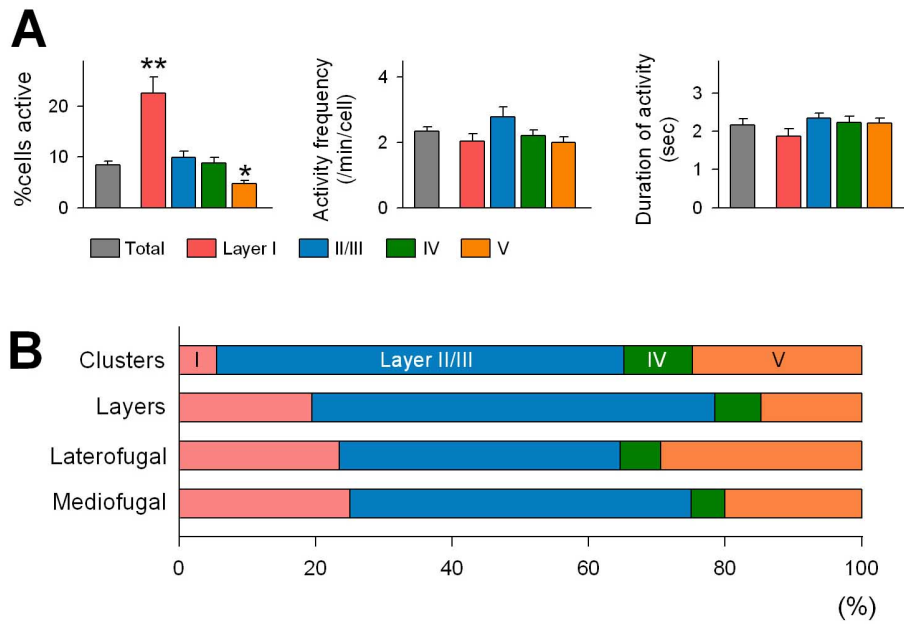


Fig. S3. Laminar analysis of spontaneous activity. (A) Percentage of active cells relative to total cells (left), the rate of activity per min (middle), and the duration of individual activity (right) as a function of cortical layer. The rate of activity was normalized by dividing the total number of detected events by the number of cells measured and by the length of movie (2 min). * $P < 0.05$, ** $P < 0.01$ vs. total; Bonferroni/Dunn test after one-way ANOVA. Data are means \pm sem. **(B)** Locations where spatially organized spike sequences emerged. Data expressed as a percentage of sequences that appeared in each layer ($n = 2,983$ motifs in 54 movies obtained from the medial prefrontal cortex).

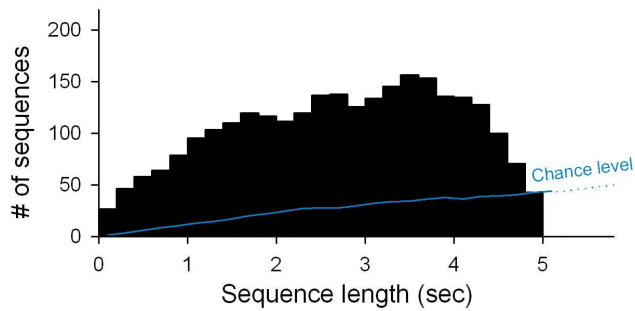


Fig. S4. Distribution of the duration of optical sequences. All 2,636 sequences detected in 54 movies are plotted. Data of 58,506 sequences in ISI-shuffled surrogates is superimposed as an average per movie (chance level). Window of analysis was 5 sec for both datasets.

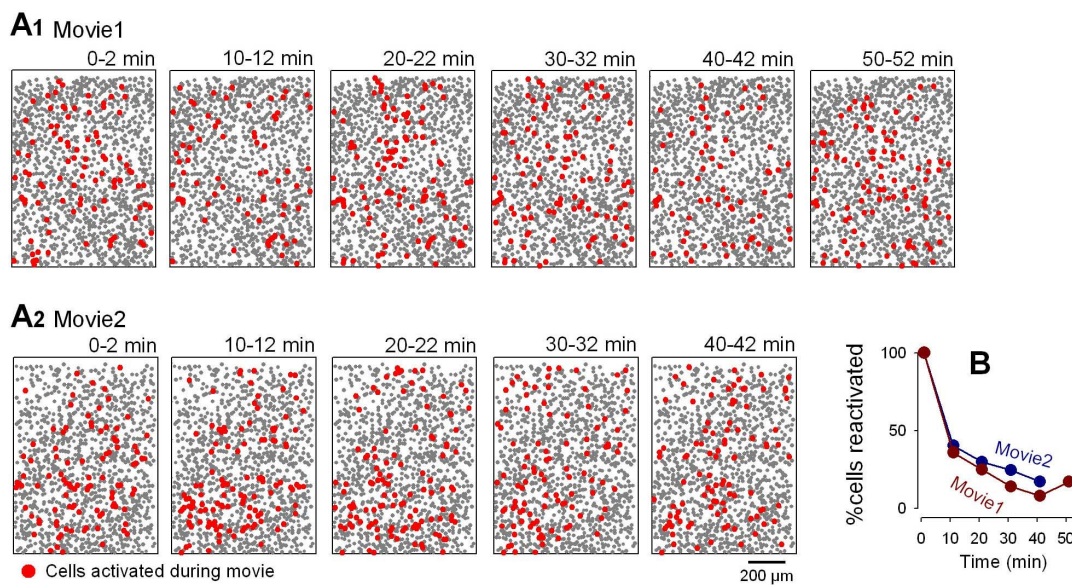


Fig. S5. Spontaneous activity drifts with time. Two examples of long-lasting imaging experiments. **(A)** Spatial maps of cells monitored. The red circles are cells activated during 2 min long movies taken every 10 min. Average percentages of active cells shared by any pair of movies were $25.9 \pm 2.4\%$ in movie 1 (ranging from 7.8% to 39.7%) and $29.6 \pm 2.2\%$ in movie 2 (ranging from 17.0% to 40.4%). **(B)** The probability that cells active during a period from 0 to 2 min were reactivated in subsequent movies declines with time.

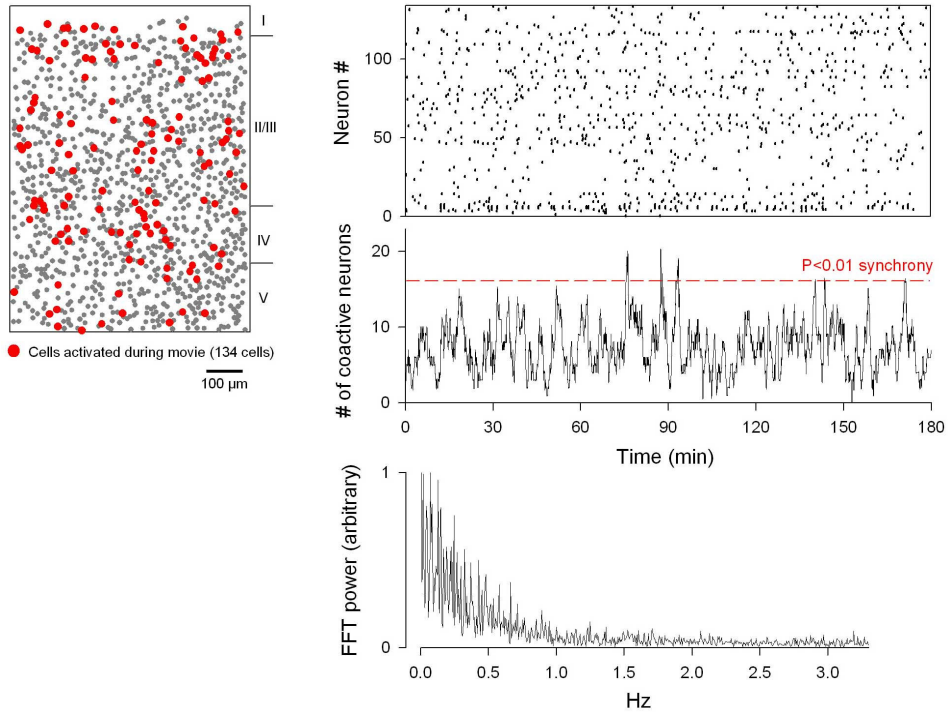


Fig. S6. Synchronization of spontaneous activity is non-periodic. Left: Locations of active cells. Right top: onset timings rasterplot. The middle histogram represents the number of cells active at each frame of the movie. Synchronization appears intermittent, and its fast-Fourier transform (FFT) indicates no apparent peaks (right-bottom).

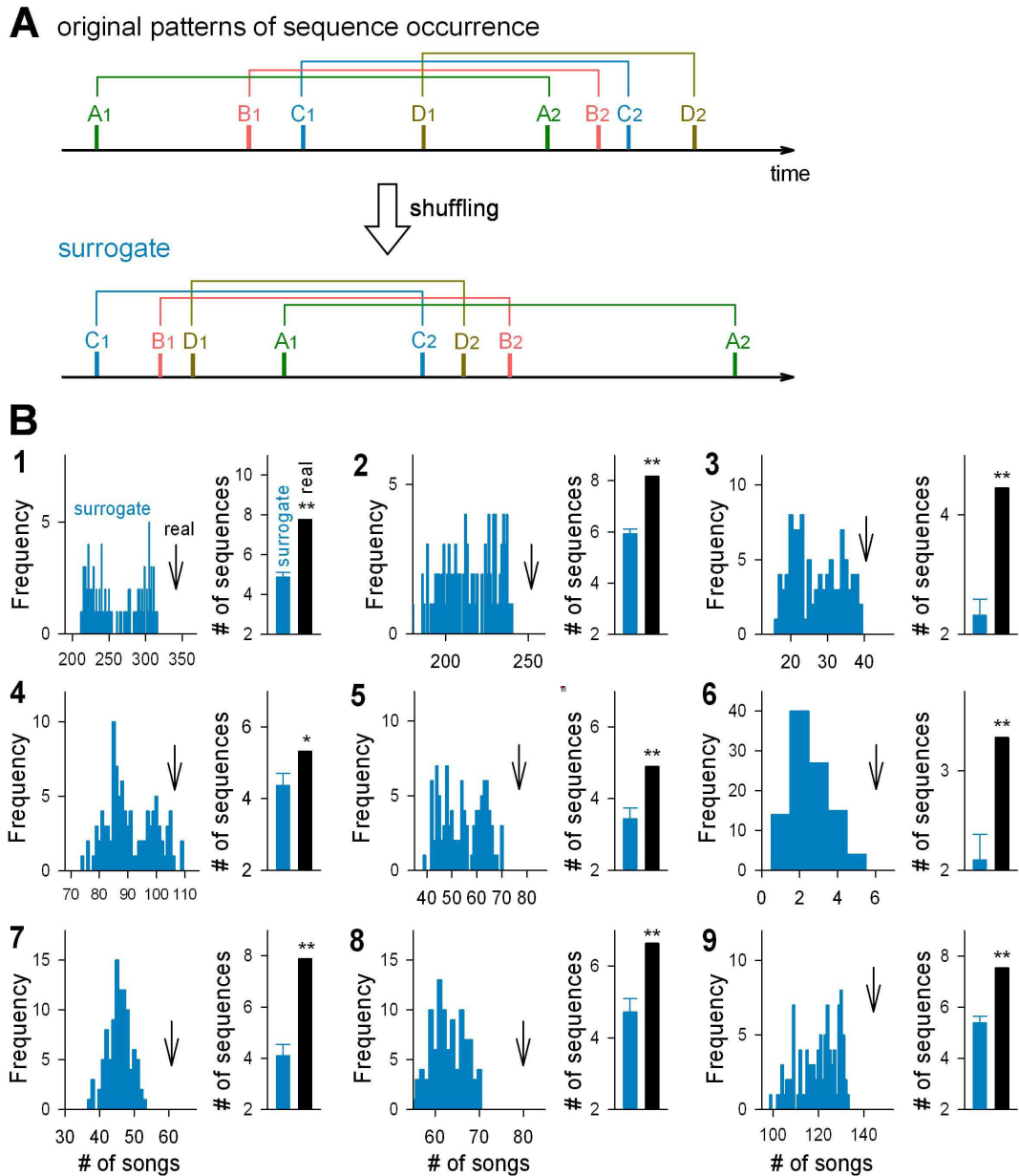


Fig. S7. Songs do not emerge by change. (A) Schematic diagram of sequence shuffling. Onset timings of sequences (A1, B1, C1, D1) and their repetitions (A2, B2, C2, D2) are randomized with maintaining each inter-sequence interval. (B) Representative analyses of 9 movies. Panels B1 and B2 originate from data of Fig. 4C and Fig. 5A-C, respectively. Shuffling was repeated 100 times. Left: blue histograms represent the number of songs detected in each surrogate. The arrows (real) indicate the number of songs in original dataset. Right: the mean numbers of sequences forming individual songs in surrogate (blue) and real (black) datasets. Data are means \pm SD of 100 surrogates. * $p < 0.05$, ** $p < 0.01$.

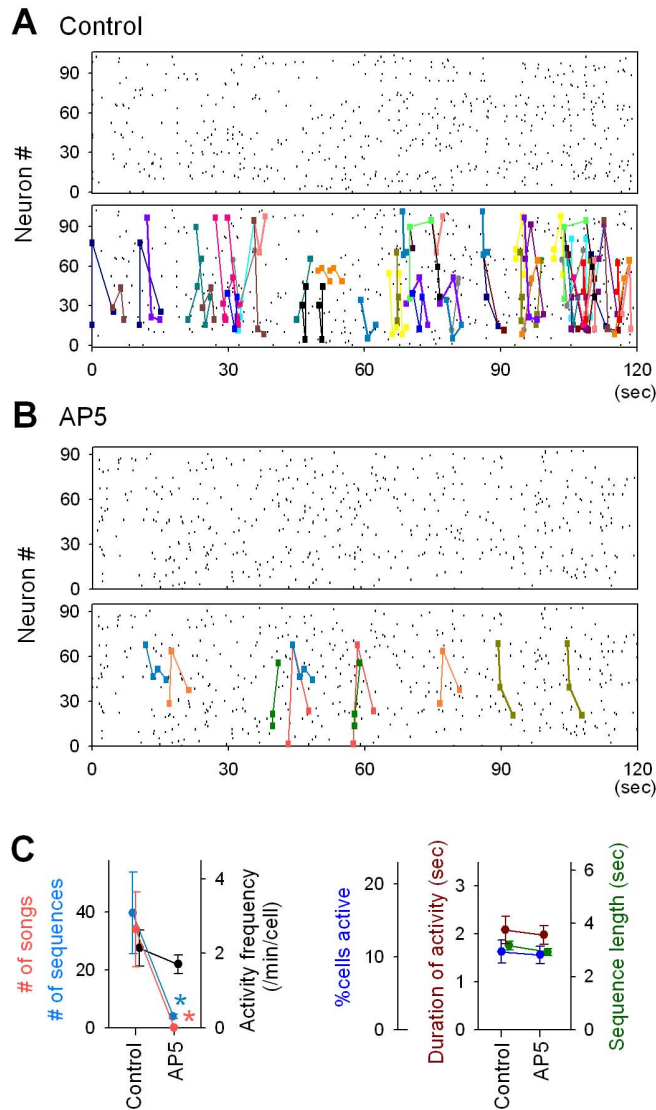


Fig. S8. NMDA receptor activity is required for song occurrence. (A-B) Each top panel indicates typical rasterplots immediately before (A) and 15 min after bath application of 50 μ M D-AP5 (B). In the bottom panels, all sequences detected are depicted on the same rasterplot (43 and 6 sequences in A and B, respectively). (C) The number of sequences (blue) and songs (red), the rate of activity (black), and the percentage of active cells to the total (dark blue), the duration of calcium transients (dark red) and the length of spike sequences (green) were monitored immediately before and 15 min after bath application of 50 μ M D-AP5. * $P < 0.05$; Wilcoxon test ($n = 7$ movies). Data are means \pm sem.

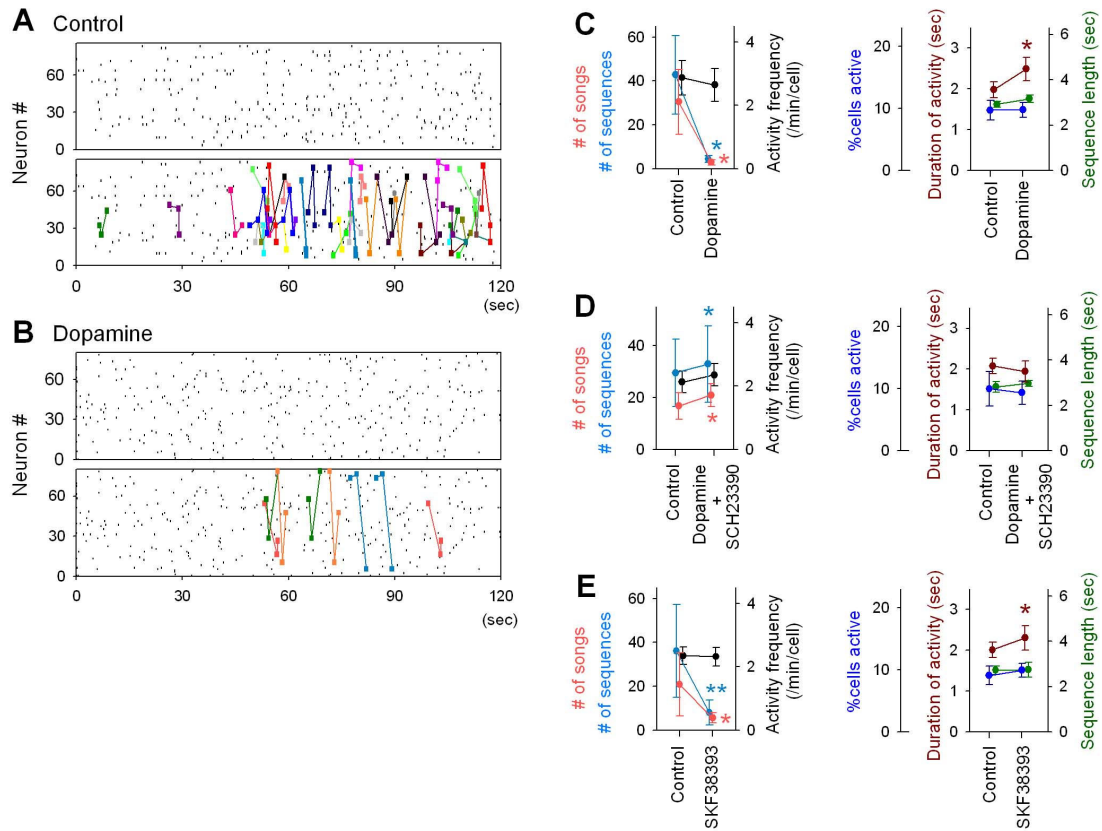


Fig. S9. Dopamine suppresses song occurrences. (A-B) Each top panel indicates typical rasterplots immediately before (A) and 15 min after bath application of 30 μ M dopamine (B). In the bottom panels, all sequences detected are depicted on the same rasterplot (24 and 4 sequences in A and B, respectively). (C-E) Effect of 30 μ M dopamine, a combination of 30 μ M dopamine (C, $n = 7$ movies) and 10 μ M SCH23390 (D, $n = 7$), and 10 μ M SKF38393 (E, $n = 6$) on the number of sequences (blue) and songs (red), the rate of activity (black), and the percentage of active cells to the total (dark blue), the duration of calcium transients (dark red) and the length of spike sequences (green). Data were obtained from the medial prefrontal cortex. The effect of dopamine in specifically blocking the temporal dynamics, without affecting the overall activity of the circuit, indicates that some of the clinical deficits present in schizophrenia can be interpreted as manifestations of an "attractor disease", since schizophrenia is believed to result, at least in part, from a pathological decline in D1-like receptor activity in the prefrontal cortex. * $P < 0.05$, ** $P < 0.01$; Wilcoxon test for the numbers of sequences and songs, paired- t test for duration. Data are means \pm sem.